

# JGR Space Physics

## RESEARCH ARTICLE

10.1029/2023JA032375

### Key Points:

- Simultaneous cosmic noise absorption and terrestrial High Frequency signal loss can be used to infer the size of D-region enhancements
- The technique described here can be scaled up to network-level providing a mechanism to resolve spatial scales of D-region enhancements

### Correspondence to:

F. Ghaly,  
filobateer.ghaly@ucalgary.ca

### Citation:

Ghaly, F., Spanswick, E., Gillies, R., Cameron, T., Skone, S., Fiori, R. A. D., & Weatherwax, A. T. (2024). Use of terrestrial high frequency signals in riometer data to explore the size of D-region electron density enhancements. *Journal of Geophysical Research: Space Physics*, 129, e2023JA032375. <https://doi.org/10.1029/2023JA032375>

Received 14 DEC 2023

Accepted 13 MAY 2024

### Author Contributions:

**Conceptualization:** E. Spanswick, R. Gillies, R. A. D. Fiori  
**Data curation:** F. Ghaly, R. Gillies, R. A. D. Fiori  
**Formal analysis:** F. Ghaly, E. Spanswick, R. Gillies, T. Cameron, R. A. D. Fiori  
**Funding acquisition:** E. Spanswick, A. T. Weatherwax  
**Investigation:** F. Ghaly, E. Spanswick, R. Gillies, T. Cameron, R. A. D. Fiori  
**Methodology:** F. Ghaly, E. Spanswick, R. Gillies, R. A. D. Fiori  
**Project administration:** E. Spanswick, A. T. Weatherwax  
**Resources:** E. Spanswick, S. Skone, R. A. D. Fiori  
**Software:** F. Ghaly, R. Gillies, T. Cameron  
**Supervision:** E. Spanswick, R. Gillies, R. A. D. Fiori  
**Validation:** F. Ghaly, R. Gillies, T. Cameron, R. A. D. Fiori  
**Visualization:** F. Ghaly, R. Gillies

© 2024 The Authors.

This is an open access article under the terms of the Creative Commons Attribution-NonCommercial License, which permits use, distribution and reproduction in any medium, provided the original work is properly cited and is not used for commercial purposes.

## Use of Terrestrial High Frequency Signals in Riometer Data to Explore the Size of D-Region Electron Density Enhancements

**F. Ghaly<sup>1</sup> , E. Spanswick<sup>1</sup> , R. Gillies<sup>1</sup> , T. Cameron<sup>2</sup>, S. Skone<sup>1</sup>, R. A. D. Fiori<sup>2</sup> , and A. T. Weatherwax<sup>3</sup>**

<sup>1</sup>University of Calgary, Calgary, AB, Canada, <sup>2</sup>Canadian Hazards Information Service, Natural Resources Canada, Ottawa, ON, Canada, <sup>3</sup>Haystack Observatory, Massachusetts Institute of Technology, Massachusetts, CA, USA

**Abstract** This paper presents the first observations from the prototype Space Weather Adaptive Network (SWAN) riometers, which are capable of simultaneous measurements of narrow-band terrestrial signal power and Cosmic Noise Absorption (CNA). We describe a methodology by which we can use coincident CNA and loss of known skywave-mode, High Frequency (HF) signals to estimate a minimum size (geographic extent) of D-region electron density enhancements. We demonstrate our technique with an example event. This methodology and early results provide a pathfinder for a continent-wide array of SWAN instruments which would be capable of utilizing multiple intersecting terrestrial HF ray paths to reconstruct the size of D-region electron density enhancements at the time of initial HF signal loss.

### 1. Introduction

The absorption of trans-ionospheric, High Frequency (HF) signals in the 20–50 MHz frequency range (often referred to as Cosmic Noise Absorption, CNA) is primarily attributed to enhanced electron density in the D-region of the ionosphere, where sufficient electron-neutral interactions make the electrons' motion collision-dominated (Budden, 1988; Hunsucker & Hargreaves, 2003). This is typically assumed to occur at altitudes of 70–100 km (Hunsucker & Hargreaves, 2003). D-region electron density enhancements can occur due to ionization from solar radiation or the precipitation of energetic protons or electrons. Solar proton events tend to have a long-lasting (possibly several days), high-level CNA signature in riometers and cover the entirety of the polar cap. The riometer signature of solar proton events is known as Polar Cap Absorption (PCA) (Hargreaves, 1969). High fluxes of protons with energies above 10 MeV can have significant impact on HF circuits at high latitudes, the spatial extent of which is determined by the proton precipitation area (Davies, 1990).

Another absorption phenomenon that affects the entire sun-lit ionosphere is known as Shortwave Fadeout (SWF). Shortly following a solar flare ( $\sim$ 8 min), Extreme Ultra-Violet and X-ray radiation enhance D-region ionization, causing significant radio-wave absorption, the levels of which depend on operating frequency, solar zenith angle, and the magnitude of the flare (Davies, 1990). SWF having both high occurrence rate per solar cycle (Fiori, Kumar, et al., 2022) and large area-of-effect implies that modeling is of great importance to HF communication and navigation systems (Chakraborty et al., 2021; Fiori, Chakraborty, & Nikitina, 2022).

In the auroral zone, absorption events often result from precipitating energetic electrons from the magnetosphere, and are known as Auroral Absorption (AA). CNA and riometers have been used for decades to explore high-energy ( $>30$  keV) electron precipitation and associated dynamics of the geospace environment. For example, substorms are known to be a significant contributor to riometer absorption (Hargreaves, 1969; Milan et al., 1994). CNA has further been used to identify enhancements to the geosynchronous  $>30$  keV electron flux and substorm dispersionless electron injections (Baker et al., 1981; Spanswick et al., 2007).

In addition to trans-ionospheric HF signal absorption, D-region electron densities can create a distinct challenge for lower-frequency (typically  $<20$  MHz), skywave-mode signals. Skywave signals are typically heavily attenuated as they tend to encounter the D region at oblique angles and have frequencies that are much more attenuated (Davies, 1990). During times of enhanced D-region electron density, there is an increase in the Lowest Useable Frequency (LUF) (Milan et al., 1998; Uryadov et al., 2019) such that these lower frequency signals are unusable. In more extreme cases, electron density enhancements may allow new propagation modes, for example, enabling Auroral-E propagation (as opposed to F-region) in the auroral oval during strong events (Blagoveshchensky &

**Writing – original draft:** F. Ghaly, E. Spanswick, R. Gillies, T. Cameron, R. A. D. Fiori

**Writing – review & editing:** F. Ghaly, E. Spanswick, R. Gillies, T. Cameron, S. Skone, R. A. D. Fiori

Sergeeva, 2020; Milan et al., 1997, 1998; Uryadov et al., 2019). Studies report electron density enhancements in the F region (higher fof2) prior to the substorm expansion phase (Blagoveshchensky & Kalishin, 2009) and magnetic storm onset (Danilov, 2013; Uryadov et al., 2019). These are among the positive storm effects, which are not detrimental to HF communications but further complicate modeling and prediction. In contrast, negative storm effects act to decrease the Maximum Useable Frequency and last long after a storm (Davies, 1990). Other effects on HF communications include off-great circle propagation and fading associated with electron density irregularities in the auroral zone (see Hunsucker & Bates, 1969 and references therein).

Statistical studies show trends in HF propagation such as diurnal features (Cameron et al., 2021; LaBelle et al., 1994; Weatherwax et al., 1994) and variation with solar cycle (Ads et al., 2015). Cameron et al. (2021) used deviations from the expected trends to show the effects of AA on HF links, therein shown as link dropouts. The effects of AA during pulsating aurora, detected by attenuation in Super Dual Auroral Radar Network echoes at 10–11 MHz, can extend over at least 4° of magnetic latitude and, on average, cover 4–5 hr of magnetic local time (MLT) (Bland et al., 2021, 2022) extended this analysis in a case study using a multi-instrument approach and showed that the region impacted by D-region electron density enhancements can extend much further in latitude range, from an L-shell of 3.7–9.6. These studies highlight the interconnected HF propagation impacts of D-region electron density enhancements. These enhancements not only produce CNA (as seen via riometers) but also dramatically impact the skywave-mode propagation (e.g., absorption, modification of propagation path).

The body of literature described above serves to highlight the dynamic nature of D-region electron density enhancements and the multiple pathways by which the terrestrial HF environment may be impacted. At any one time, the spatial structuring of D-region absorption can be driven by ionization due to radiation (e.g., due to a strong solar flare or Bremsstrahlung radiation) or precipitation mechanisms associated with the magnetospheric particle population. Early observations concerning the spatial extent of the absorption region summarized by Hunsucker and Hargreaves (2003) indicate that finer structure absorption can be part of a larger distribution of patches that extend a few 100 kms in both north–south and east–west directions. The overall distribution of spatial extent, however, shows no general consensus across different events, ranging from 10 to 800 km and 90–800 km in the north–south and east–west directions, respectively. The plethora of magnetospheric precipitation mechanisms convolved with magnetospheric energization and transport leads to significant variability between events in terms of signatures observed in riometers (Berkey et al., 1974; Jones et al., 2011), even when grouped by their occurrence in different MLT sectors (Kainuma et al., 2001). Even within the morning sector, there seems to be high variability in terms of absorption patch shape, elongation dimension, and drift direction (Makarevitch et al., 2004). The complexities and variability of absorption events highlight the importance of observations that can resolve spatial structuring in D-region electron density enhancements.

In this paper, we present a methodology for modeling the absorption region employing next-generation, Space Weather Adaptive Network (SWAN) riometers which feature a wide bandwidth, enabling the reception of skywave-mode terrestrial transmissions. We present a case study, where CNA is coincident with a dropout in terrestrial signals and utilize the loss of terrestrial signals from known sources during the onset of absorption to map out the absorbing region beyond the riometer's nominal Field-of-View (FOV). This study provides a simple methodology, which as the SWAN network expands, can be utilized to provide key observations of the initial spatial scale of D-region electron density enhancements, at the time of HF signal loss.

## 2. Data

### 2.1. Hyperspectral Riometer Data

SWAN riometers, also known as Hyperspectral Riometers (HSRs), are newly designed digital systems that will replace the existing Geospace Observatory Canada (GO-Canada) network of analog, single-beam, 30-MHz riometers operated by the University of Calgary. Both HSRs and GO-Canada riometers used in this study are shown in Figure 1. The HSRs leverage a radio astronomy antenna (the Long Wavelength Array, LWA, antenna), coupling it to a custom-designed receiver, incorporating a Field Programmable Gate Array. The system employs customizable signal acquisition and processing, affording a flexibility and observational frequency range beyond typical multi-frequency riometers. Data from three prototype systems, installed between August 2021 and February 2023, are used in this study. These HSRs are located in Meanook (MEAN), Rabbit Lake (RABB) and Meadow Lake (MEDO). Figure 1 shows the FOV of these HSRs.

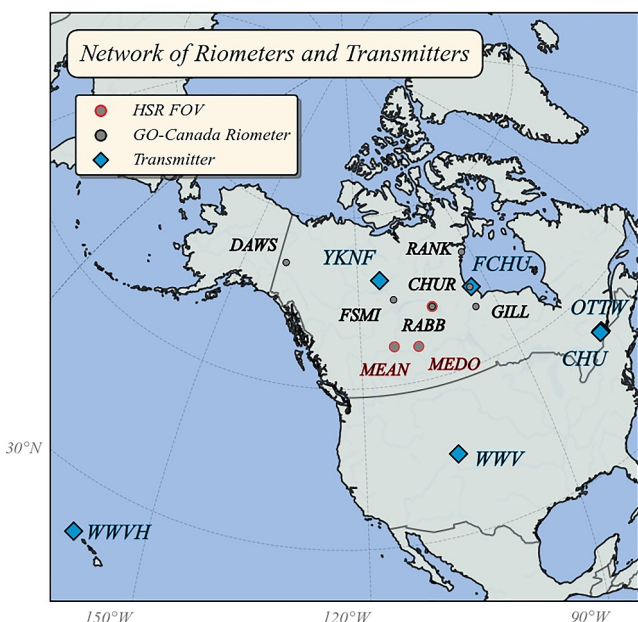


**Figure 1.** Map showing the network of instruments utilized in this study. Instrument identifiers and exact locations are listed in Table 1. Hyperspectral Riometer (HSR) FOVs projected to 85 km are shown as gray circles with red boundaries. Go-Canada riometers are shown as gray circles with black boundaries. NRC's CHU timing-signal transmitter overlaps with NRCan's OTTW transmitter, and Go-Canada's CHUR riometer overlaps with NRCan's FCHU transmitter on the map due to proximity. Both an HSR and a GO-Canada riometer coexist at Rabbit Lake (RABB).

two HSR frequency bins. The diurnal behavior of the terrestrial signals displays characteristics of skywave mode propagation. Namely, the lower/higher LUF during local night/day (Davies, 1990). For MEAN, magnetic local midnight is at ~08:20 UT, the time at which (for the date shown in Figure 2) the riometer observes terrestrial signals down to approximately 1 MHz. At magnetic local noon (~20 UT) terrestrial transmissions are observed at frequencies above ~18 MHz.

Other terrestrial signals appear to be high-power and constant throughout the day. These specific signals are interpreted as being transmitted close to the location of the riometer and having a line-of-sight path to the antenna

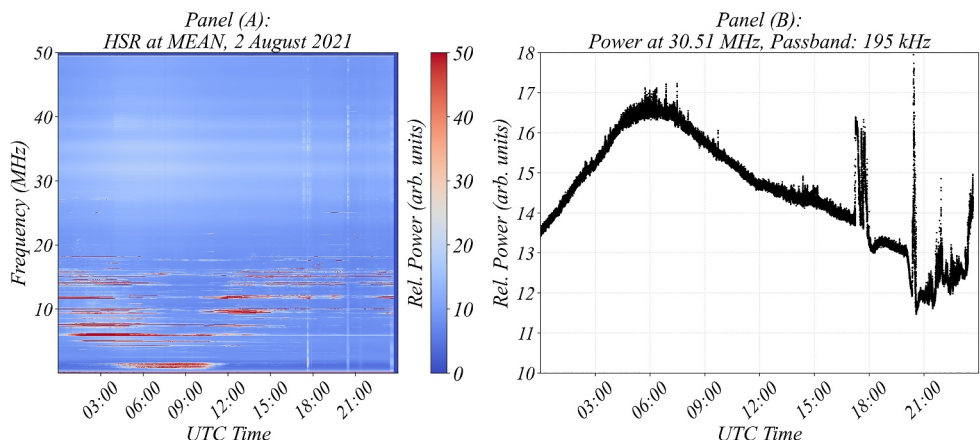


**Figure 2.** Panel (a) (left) shows full spectrum data for signals in the range 0.01–49.50 MHz from an Hyperspectral Riometer at Meanook (MEAN). Panel (b) (right) shows observed power in a 195 kHz (16 bins) passband centered around 30.51 MHz as a function of time.

**Table 1***Site Codes, Locations and Coordinates for Instruments Utilized in This Study*

| Site code                                                    | Location                           | Geodetic latitude (°) | Geodetic longitude (°) |
|--------------------------------------------------------------|------------------------------------|-----------------------|------------------------|
| <b>Riometers</b>                                             |                                    |                       |                        |
| <i>Hyperspectral Riometers (HSRs)</i>                        |                                    |                       |                        |
| RABB                                                         | Rabbit Lake, Saskatchewan          | 58.23                 | -103.68                |
| MEAN                                                         | Meanook, Alberta                   | 54.62                 | -113.35                |
| MEDO                                                         | Meadow Lake, Saskatchewan          | 54.13                 | -108.51                |
| <i>Go-Canada Riometers</i>                                   |                                    |                       |                        |
| DAWS                                                         | Dawson City, Yukon                 | 64.05                 | -139.11                |
| RANK                                                         | Rankin Inlet, Nunavut              | 62.82                 | -92.11                 |
| FSMI                                                         | Fort Smith, Northwest Territories  | 60.03                 | -111.93                |
| CHUR                                                         | Fort Churchill, Manitoba           | 58.76                 | -94.09                 |
| RABB                                                         | Rabbit Lake, Saskatchewan          | 58.23                 | -103.68                |
| GILL                                                         | Gillam, Manitoba                   | 56.38                 | -94.64                 |
| <b>Transmitters</b>                                          |                                    |                       |                        |
| <i>Natural Resources Canada (NRCan)</i>                      |                                    |                       |                        |
| YKNF                                                         | Yellowknife, Northwest Territories | 62.48                 | -114.48                |
| FCHU                                                         | Fort Churchill, Manitoba           | 58.74                 | -93.82                 |
| OTTW                                                         | Ottawa, Ontario                    | 45.41                 | -75.55                 |
| <i>National Institute of Standards and Technology (NIST)</i> |                                    |                       |                        |
| WWV                                                          | Boulder, Colorado                  | 40.43                 | -105.68                |
| WWVH                                                         | Kauai, Hawaii                      | 21.98                 | -159.75                |
| <i>National Research Council (NRC)</i>                       |                                    |                       |                        |
| CHU                                                          | Ottawa, Ontario                    | 45.30                 | -75.76                 |

*Note.* Note that NRCan's OTTW transmitter is close to NRC's CHU transmitter in Ottawa, Ontario. Also note that an HSR and a Go-Canada riometer coexist at Rabbit Lake (RABB).

(e.g., airport beacons, local repeaters, etc.). We note that the riometer receiver does not support decoding of terrestrial signals, or determining direction of arrival, but does allow for total received power to be monitored as a function of time at the cadence of the riometer. It is the system's filtering (as a function of frequency) and the antenna directional gain pattern that allow for relatively weak overhead cosmic signals to be measured with the same system as the much stronger terrestrial transmissions that enter lower gain regions of the antenna directional pattern.

## 2.2. HF Transmitters

We utilize a network of HF transmitters, see Table 1 and Figure 1. Natural Resources Canada (NRCan) has installed transmitters in Ottawa (OTTW), Yellowknife (YKNF) and Fort Churchill (FCHU). These transmitters operate at 5.3820, 6.9285, 8.0995, 10.4220, 11.1070, and 14.3644 MHz, cycling through all 6 frequencies on a prearranged schedule that repeats every 7.5 min (see Cameron et al., 2021).

Timing-signal transmitters were also utilized in this study. The National Research Council's CHU transmitter (Canada, 2019) is located close to NRCan's OTTW transmitter (see Table 1), and hence both overlap in Figure 1. The CHU transmitter operates at 3.33 and 14.67 MHz at 3 kW and at 7.85 MHz at 5 kW. In addition, the National Institute of Standards and Technology has two high-power transmitters sending timing signals, located in Boulder, Colorado (call sign WWV) and Kauai, Hawaii (call sign WWVH) (Nelson et al., 2005). Both WWV and WWVH operate at 5, 10, and 15 MHz at 10 kW. WWV additionally transmits at 2.5, 20, and 25 MHz, albeit at 2.5 kW radiated power, and WWVH transmits at 2.5 MHz at 5 kW (see <https://www.nist.gov/pml/time-and-frequency-division/time-distribution/radio-station-wwv>).

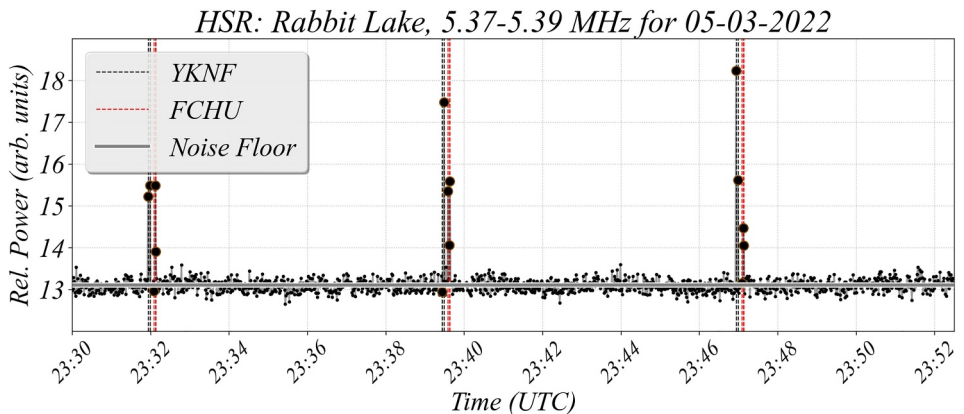


**Figure 3.** One-second power measurements from the Hyperspectral Riometer at Rabbit Lake (RABB) in the 5.37–5.39 MHz frequency range (black dots). Times of the 5.382 MHz transmissions from the Natural Resources Canada transmitters at Yellowknife (YKNF) and Fort Churchill (FCHU) are shown as vertical lines (black and red, respectively). The noise floor at this frequency, for this period, is indicated with the horizontal gray line.

### 2.3. Identification of Terrestrial HF Signal Source

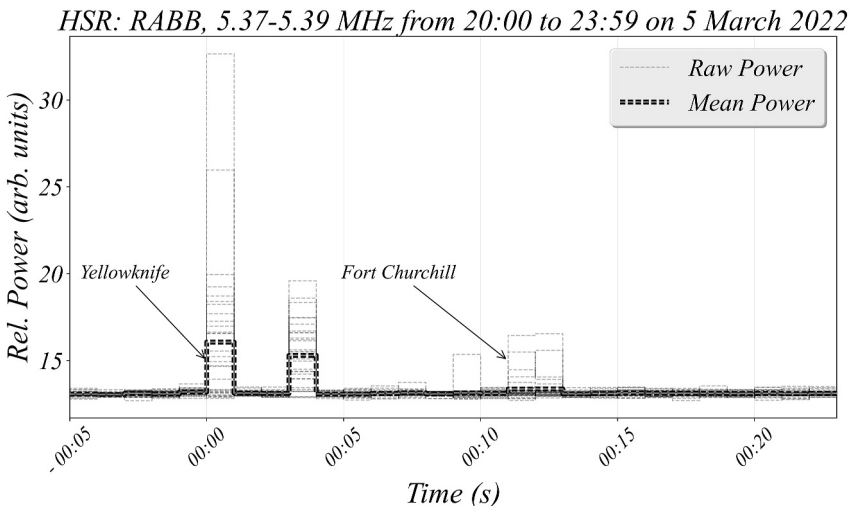
Utilizing the relevant Canadian/United States frequency allocation information (see [https://sms-sgs.ic.gc.ca/eic/site/sms-sgs-prod.nsf/eng/h\\_00010.html](https://sms-sgs.ic.gc.ca/eic/site/sms-sgs-prod.nsf/eng/h_00010.html), <https://www.ntia.doc.gov/category/spectrum-management>) and analysis of the temporal behavior of the acquired power (matching chirp patterns of known transmitters), it is possible to confirm some signal sources within the lower frequency riometer data, facilitating the study presented here.

Figure 3 shows 22.5 min of HSR data from RABB for a single frequency bin, 5.37–5.39 MHz taken on 5 March 2022. The only listed active transmitters in this frequency band are associated with the NRCan transmitter network. During this timeframe, the YKNF and FCHU transmitters were active with offset transmission schedules. The transmission schedule active during 5 March 2022 is shown in Table 2. YKNF and FCHU start transmitting at 01:55 and 02:05 at the start of every UT hour, repeating every 7.5 min and resulting in 8 cycles every hour. Within each cycle the YKNF transmitter produces two half-second pulses, 2 seconds apart, followed, 6 s later, by the FCHU transmitter, which transmits a single, half second pulse followed by a two-second Barker code transmission one second later. We note the FCHU transmitter clock was not GPS locked during this interval, so the timing of the pulse is less precise than YKNF. The times of the known transmissions are indicated in Figure 3 with dashed vertical lines (black lines indicate the schedule of YKNF and red indicates the schedule for FCHU). Individual power levels in the 5.37–5.39 MHz band (one per second) recorded by the riometer are shown as black dots.

**Table 2**  
Natural Resources Canada Transmission Schedule Active During 5 March 2022

| Frequency (MHz) | Transmission Start Time (UTC) |       |       |       |       |       |       |       |       |  |
|-----------------|-------------------------------|-------|-------|-------|-------|-------|-------|-------|-------|--|
|                 | YKNF                          |       |       | FCHU  |       |       | OTTW  |       |       |  |
| 5.3820          | 01:55                         |       |       |       | 02:05 |       |       |       |       |  |
| 6.9285          |                               | 04:25 |       |       |       | 04:35 |       |       |       |  |
| 8.0995          | 00:00                         | 02:30 | 05:00 | 00:10 | 02:40 | 05:10 | 00:15 | 02:45 | 05:15 |  |
| 10.4220         | 06:55                         |       |       |       | 07:05 |       |       | 07:10 |       |  |
| 11.1070         | 00:35                         | 03:05 | 05:35 | 00:45 | 03:15 | 05:45 | 00:50 | 03:20 | 05:50 |  |
| 14.3644         | 01:10                         | 03:40 | 06:10 | 01:20 | 03:50 | 06:20 | 01:25 | 03:55 | 06:25 |  |

*Note.* The transmission start times are staggered. Yellowknife (YKNF) is always ahead of Fort Churchill (FCHU), which is ahead of Ottawa (OTTW). This schedule starts at the beginning of each hour and repeats every 7.5 min (resulting in 8 cycles every hour). During this time OTTW was not transmitting at both 5.3820 and 6.9285 MHz.



**Figure 4.** Superposed epoch analysis of riometer power at Rabbit Lake (RABB) in the 5.37–5.39 MHz band for 32 successive Natural Resources Canada transmission cycles. Zero time is the time of the Yellowknife transmission. The timing of the Fort Churchill transmissions within the cycle is also shown. Churchill transmits 10 s after Yellowknife (first transmission).

Riometer power measurements in this band are seen to increase well above the noise floor (indicated with a gray line and calculated as the tenth percentile of power measurements during the 22.5-min period shown) during the times the YKNF and FCHU transmitters are scheduled to transmit. If the riometer measures an increase in power consistent with the known transmission schedule (as shown above), we argue that this is evidence that the riometer is, in fact, receiving the skywave mode transmission from (in this case) YKNF and FCHU. We note that the exact timing and length of the pulses is limited by the riometer data acquisition cycle, which integrates over one-second periods. If the 0.5 s pulse is misaligned with the acquisition cycle, the riometer power increase will be observed across two temporal samples and in general have less power in each sample.

To further explore the riometer response to the known NRCAN signals, we perform a superposed epoch analysis of the riometer power, relative to the known transmission time. In Figure 4 4 hr of riometer data are analyzed. The data are time-shifted so that each transmission cycle (as shown in Table 2) starts at the YKNF transmission (second 00:00 in Figure 4). This was done to examine all the pulses from the NRCAN transmitters during this time and confirm that each transmission was received at the appropriate time. Over the 4 hr period shown, 32 transmission cycles are considered. Figure 4 shows distinct peaks in average riometer power from 0 to 1 s and 3 to 4 s following the known NRCAN pulse transmissions from YKNF, followed by a lower power peak associated with the FCHU transmission cycle. The average (mean) power in this case is taken across transmission cycles.

The above analysis shows that the riometer response in terrestrial bands associated with the NRCAN transmission cycle matches the transmission schedule. The peaks in observed power align with the prescribed NRCAN transmission cycle (see Table 2). This provides confidence for interpreting the geographic origin of signals based on timing. Based on this, we assert that the temporal match between enhanced riometer power within a single riometer frequency bin, and the known schedule for transmissions within that frequency band is evidence that the riometer received a signal from that source location. In the case highlighted in Figure 4, we argue that the riometer at RABB received the YKNF and FCHU transmissions.

If the transmitter sequence is unknown, then the argument for conclusive reception of a signal becomes weaker. In these cases, we solely rely on the list of registered transmitters and their self-declared transmission power. Figure 5 shows an example for the continuous, high-power, WWV/WWVH transmissions in the 10 MHz band, for which the HSR at MEAN observe near-continuous power above the noise floor.

#### 2.4. Simultaneous Cosmic Absorption and Loss of Terrestrial HF Transmissions

During prototype testing, it was observed that absorption of cosmic radio signals (in the 25–50 MHz range) could occur near simultaneously with loss of some terrestrial signals (seen in the <25 MHz data). Figure 6 shows one example of this behavior from an HSR at Meanook, Alberta on 13 March 2022. In general, these events indicate a

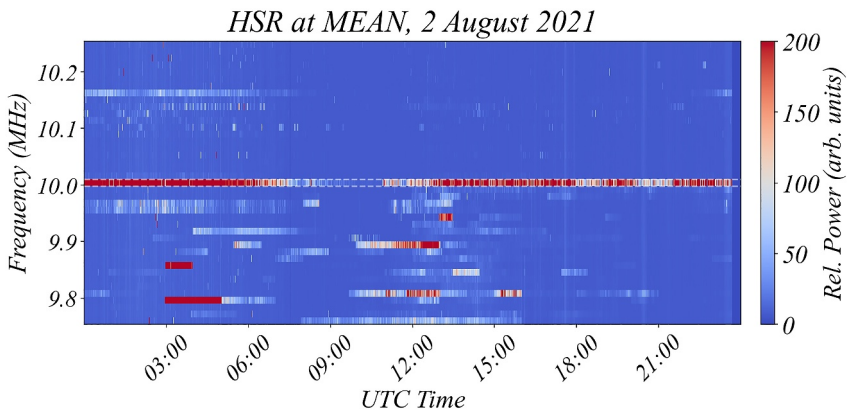


**Figure 5.** Example riometer spectrum from Meanook (MEAN) for, 2 August 2021, showing the frequency range 9.75–10.25 MHz. The WWV/WWVH transmission at 10.00 MHz is identified (bordered by white dashed lines).

change to the radio wave propagation environment such that higher-frequency signals from overhead (e.g., the Galactic noise) are impacted as well as the lower-frequency, skywave-mode, terrestrial signals. While the observation of this correlation has been well documented (see Hargreaves, 1969 and references within; Hunnsucker & Hargreaves, 2003; Milan et al., 1994, 1998; Uryadov et al., 2019), here we describe a methodology to utilize the simultaneous absorptions to inform estimates of the size of the absorbing region.

Figure 7 shows three additional examples of similar events observed across the prototype network with varying levels of activity indicating the common nature of these observations. In this paper, we highlight one event at MEDO on 21 February 2023, and conduct detailed analysis to support determination of the minimum size of the D-region electron density enhancement (assumed here to be responsible for impacts on HF terrestrial propagation and CNA).

### 3. Methodology

As described above, it is possible to identify the status of a few HF links within the HSR data. For NRCAn transmitters, we identify the signal based on the known transmission schedule and frequencies. For other

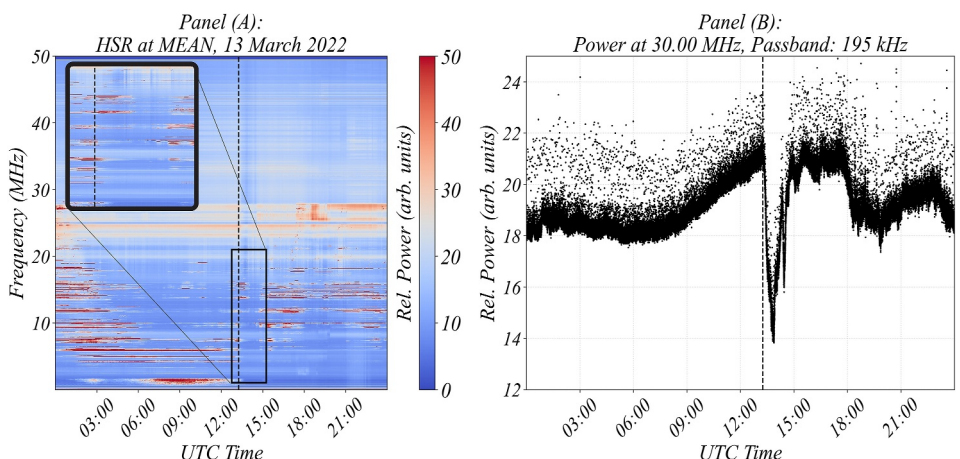


**Figure 6.** Riometer measurements from Meanook (MEAN) on 13 March 2022. Panel (a) (left) shows the full spectrum, from 0.01 to 49.50 MHz. An absorption event (loss of High Frequency (HF) power) marked with a vertical dashed line begins at approximately 13:15 UT. The sub-panel shows the distinct loss of terrestrial HF signals at the dashed line. Panel (b) is the equivalent riometer signal of a 30 MHz, single channel riometer, derived from the multi-frequency data. The cosmic absorption is marked with the same dashed line. The inset axis shows power for signals with frequencies ranging from 1 to 21 MHz.

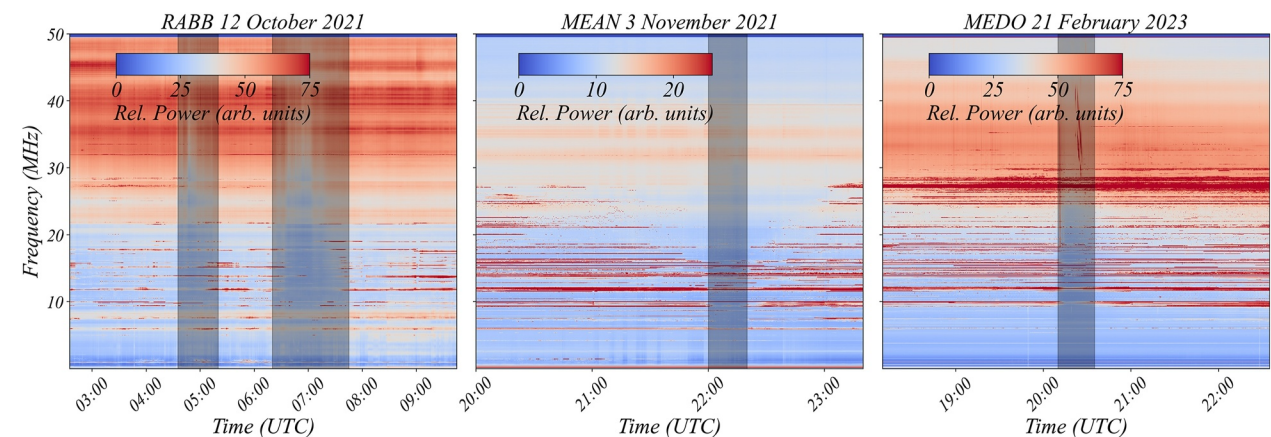


**Figure 7.** Example events from each of the Hyperspectral Riometers from the prototype network. Highlighted in gray are times when Cosmic Noise Absorption was simultaneous with loss of terrestrial signals. We focus on MEDO 21 February 2023 (right-most plot) for applying our methodology.

transmitters, namely WWV, WWVH, and CHU, we rely on monitoring the power within an appropriate frequency band.

We note that while a matching signal sequence (meaning riometer power mimics the transmitter schedule) is argued here as conclusive evidence of an available HF link, the reverse is not necessarily true. A lack of signal acquisition in the riometer, in general, cannot be strictly interpreted as an unavailable link. There are many reasons why the riometer would not receive a particular HF signal, most notably that the signal was not transmitted. Since we cannot confirm that signals are transmitted, we restrict ourselves here to times in which the riometer has acquired the signal, then lost the signal, then reacquired the signal. In these cases, we argue that the loss was not due to lack of transmission, but rather changes to the HF propagation environment.

In this study we are concentrating on events in which terrestrial signal loss is observed simultaneously with CNA. Under these conditions, the CNA provides critical information about the state of the D-region. The subsequent enhancement of D-region electron density is nominally assumed to be at altitudes of 70–100 km. During a time of coincident CNA and terrestrial signal loss, we therefore attribute the terrestrial loss to an enhanced electron density layer overhead at the riometer location. We assert this is reasonable due to the simultaneity of the response seen in the data. It is also supported by the fact that radio wave absorption is proportional to the inverse of the square of the signal frequency (see e.g. Hunsucker & Hargreaves, 2003). For example, if there are 3 dB of absorption at 30 MHz (in the cosmic band), one would expect 108 dB of absorption at 5 MHz if the signals are transiting the same region (our primary assumption). Additionally, while most signals in the 30 MHz band are extra-terrestrial and trans-ionospheric, the double (or multiple) traversal of low-frequency HF signals of the D region, combined with their oblique trajectories in that region on their way to the riometer, results in higher absorption (Hargreaves, 1969). The broad frequency range of the signal losses (see Figure 7) also adds credibility to our assumption, since if terrestrial loss were associated with effects further away, we would anticipate some signals remaining in the riometer measurements during the event (since they are coming from other directions).

Under the assumption that a single layer of enhanced electron density is responsible for both the CNA and terrestrial loss, we utilize raypath simulations to model where the signals encounter this layer. Figure 8 shows an example raypath simulation for one known signal, the 15 MHz signal from the WWV transmitter observed in the MEDO HSR. Utilizing electron density profiles from the International Reference Ionosphere model (IRI) (Froí et al., 2020) and the Provision of High-Frequency Raytracing Laboratory for Propagation Studies (PHaRLAP) toolbox, we simulate the pre-event raypath that facilitated signal reception by the riometer. This is a baseline simulation that identifies the relevant ionospheric path prior to any absorption.

Ray tracing simulations identify the pathways by which a terrestrial transmission (characterized by an initial location, frequency, and azimuth) reaches the HSR. We note that this simulation, since it utilizes IRI, is done at a time prior to the onset of any absorption during a precipitation event. Our methodology makes the simple assumption that there are two states to the signal propagation, one (modeled) in which the signal can reach the

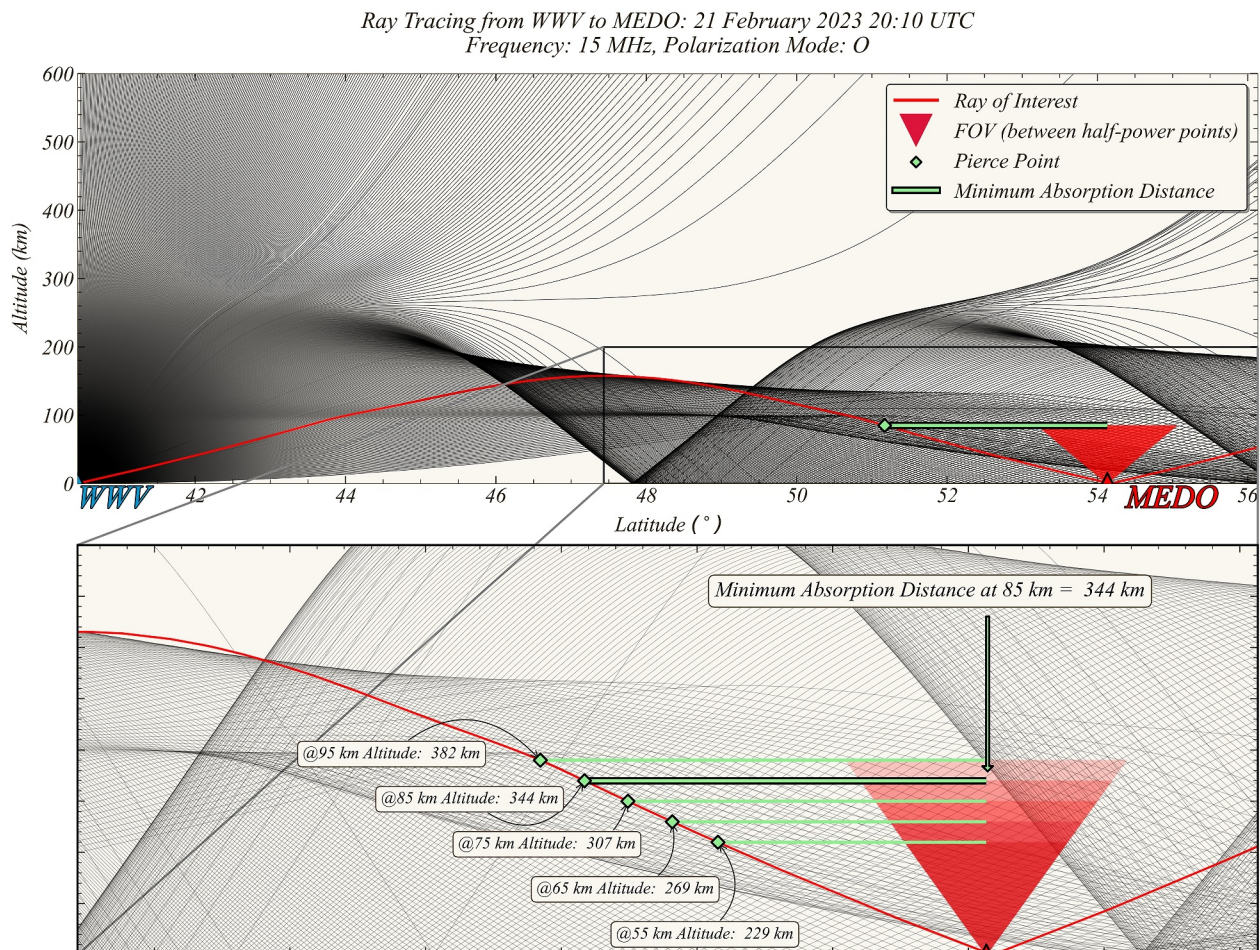


**Figure 8.** Simulation of ray paths for a signal at 15.00 MHz transmitted from WWV at a range of elevation angles along an azimuth toward Meadow Lake (MEDO). The raypath that reaches MEDO is plotted in red. The FOV, a cone enclosing the half-power points of the antenna's radiation pattern, of the MEDO Hyperspectral Riometer (HSR) is shown in red at the HSR site, terminating at the assumed absorbing altitude of 85 km. The minimum size of the absorbing region (shown as a green extension from the center of the cone) is assumed to be the distance from the center of the HSR's FOV to the pierce point of the red ray at 85 km altitude. For comparison, the inset figure shows absorption distances and FOV projections at 55, 65, 75, 85, and 95 km altitudes.

riometer, and one in which the signal cannot reach the riometer. We assume that the only difference between these two states is the absorbing layer. While the evolution of the ionospheric electron density can modify the signal path, for simplicity we assume here that the path is unchanged. We use the pre-absorption ray tracing simulation to identify the intersection (pierce points) of the raypath with the assumed altitude of the absorbing layer, situated at 85 km. This method informs us how far from the riometer the absorbing layer would need to be to impact the raypath. Different altitudes and their respective absorption distances are shown in Figure 8. For this HF link, the average difference in absorption distances between 55, 65, 75, 85, and 95 km altitudes for the assumed layer is about 38 km across the sky per 10 km difference in altitude. Shown in Table 3 are absorption distance at a given altitude, average difference between absorption distances and range of absorption distances for all HF links used in this study. The choice of 85 km altitude is due to the nature of the event and discussed in Section 5.

This simple method establishes the minimum size of the absorbing region—defined as the extension of the HSR FOV projected to 85 km altitude to the pierce point of the ray and is valid for the direction between the riometer and the transmitter. With multiple riometers and multiple transmitters, there is potential for this method to inform and constrain the size of D-region enhancements. In the following section we detail this methodology for our example event on 21 February 2023, for which two HSRs (MEAN and MEDO) both observed CNA coincident with terrestrial signal loss. We note that for this event, the RABB HSR was experiencing technical difficulties and as such we are not confident in its interpretation.

**Table 3**

Absorption Distances at 55-, 65-, 75-, 85-, and 95-Km Altitudes for Every Transmitter-HSR Link Investigated for This Event

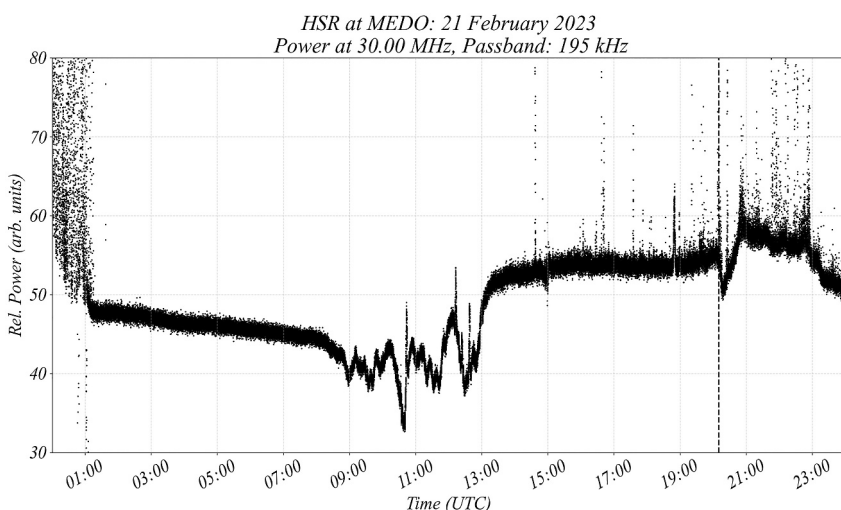
| Transmitter | Frequency (MHz) | 55 (km) | 65 (km) | 75 (km) | 85 (km) | 95 (km) | Average difference (km) | Range of distances (km) |
|-------------|-----------------|---------|---------|---------|---------|---------|-------------------------|-------------------------|
| HSR: MEAN   |                 |         |         |         |         |         |                         |                         |
| OTTW        | 11.107          | 149     | 174     | 199     | 223     | 248     | 25                      | 99                      |
| WWV         | 10.000          | 119     | 141     | 163     | 184     | 206     | 22                      | 87                      |
| WWV         | 15.000          | 96      | 113     | 130     | 148     | 165     | 17                      | 69                      |
| WWVH        | 15.000          | 223     | 255     | 286     | 317     | 349     | 31                      | 125                     |
| CHU         | 14.670          | 215     | 251     | 287     | 322     | 357     | 36                      | 143                     |
| HSR: MEDO   |                 |         |         |         |         |         |                         |                         |
| OTTW        | 11.107          | 94      | 110     | 126     | 142     | 158     | 16                      | 64                      |
| WWV         | 10.000          | 115     | 135     | 155     | 175     | 195     | 20                      | 79                      |
| WWV         | 15.000          | 229     | 269     | 307     | 344     | 382     | 38                      | 153                     |
| WWVH        | 15.000          | 269     | 314     | 358     | 400     | 443     | 44                      | 174                     |
| CHU         | 14.670          | 99      | 115     | 131     | 147     | 163     | 16                      | 64                      |

Note. The average difference is the mean of the differences between absorption distances at the chosen altitudes (e.g., the mean of 40, 38, 37, and 38 km for the WWV-MEDO link at 15 MHz). The range is the maximum minus the minimum of those distances.

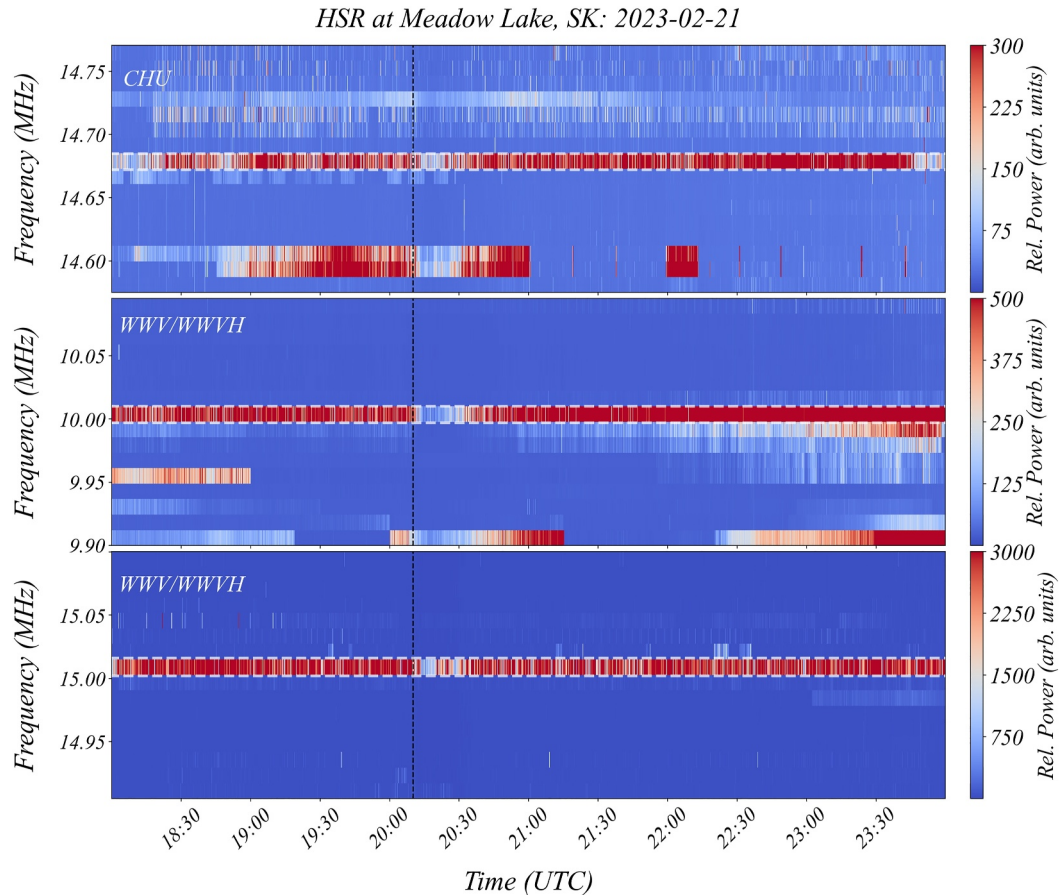
#### 4. Event Study: 21 February 2023

Figure 9 shows a single day of data from the prototype HSR at MEDO at the 30 MHz single channel. This day contained multiple absorption events, with associated changes to the terrestrial HF signals acquired by the riometer. While we note the large, dynamic changes occurring in the morning sector, here we choose to focus on the isolated absorption event in the post-noon sector ( $\sim$ 20 UT) due to the simplicity of the absorption signature. The earlier riometer signatures between  $\sim$ 8 and 13 UT are that of AA, marked by their temporal irregularities and may be observed in optical data (not shown here). The latter is a SWF event associated with a class-M5 solar flare. The remaining analysis in this section will focus on the SWF event, the onset of which is marked with a dashed line in Figure 9.

Coincident with the reduction in cosmic power, is a reduction in terrestrial signals in the lower ( $<25$  MHz) bands. Figure 10 shows the CHU signal from an Ottawa transmitter at 14.67 MHz and the 10 and 15 MHz transmissions from WWV/WWVH. The reduction in observed power from the CHU and WWV/WWVH transmitters is



**Figure 9.** An absorption event on 21 February 2023. Hyperspectral Riometer measurements taken from Meadow Lake (MEDO). Shown is the observed power at 30 MHz, with a passband of 195 kHz. The dashed line indicates the onset used in mapping the absorption region.



**Figure 10.** Spectra showing terrestrial transmissions for the 21 February 2023 event as observed by the Meadow Lake (MEDO) Hyperspectral Riometer. In order from top to bottom are plots showing the 14.67 MHz transmission by CHU, followed by 10 and then the 15 MHz transmissions by WWV/WWVH. The appropriate frequency bin is bordered by white dashed lines. Observed is simultaneous reduction of power for these terrestrial transmissions at the onset of absorption marked by the black dashed line.

consistent with the onset of the absorption at 30 MHz (dashed vertical line). For our methodology presented here, we are not considering the few minutes around the onset of signal loss and are assuming a binary state of the D-region, quiet (pre-absorption) and enhanced (associated with cosmic absorption). In future work, event-based modeling could utilize finer timing of various HF signal losses to explore ionospheric electron density changes during dynamic events. However, for demonstration of our methodology we here use a binary state, where the two states are a) quiet or b) enhancing or absorbing.

Figure 11 shows the coincident loss of the NRCan signal from OTTW at the 11.1070 MHz band as observed in the 11.1084 MHz bin of the MEDO HSR. For this frequency band, we could not confirm the reception of transmissions from either YKNF or FCHU before the absorption onset— which was also the case for the other NRCan transmission frequencies.

Figure 12 shows the output of the pierce point analysis for the combined CNA and terrestrial signal loss of the 4 transmitters analyzed in the MEDO data for this event. Figure 13 shows absorption measurements from GO-Canada riometers for the day of the event. The GO-Canada riometer at RABB, having the lowest solar zenith angle at the time of the event, shows the highest peak absorption (0.67 dB), while both DAWS and RANK, being the farthest away from the subsolar point, have the lowest peak absorption. GO-Canada riometers with peak absorption higher than or about 0.5 dB have been utilized in the mapping in Figure 14. Figure 14 is the combined MEAN and MEDO pierce point analysis for the available terrestrial links in each of their data. We note the clustering of the pierce points provides confidence as to the boundary of the absorbing layer. More pierce points in

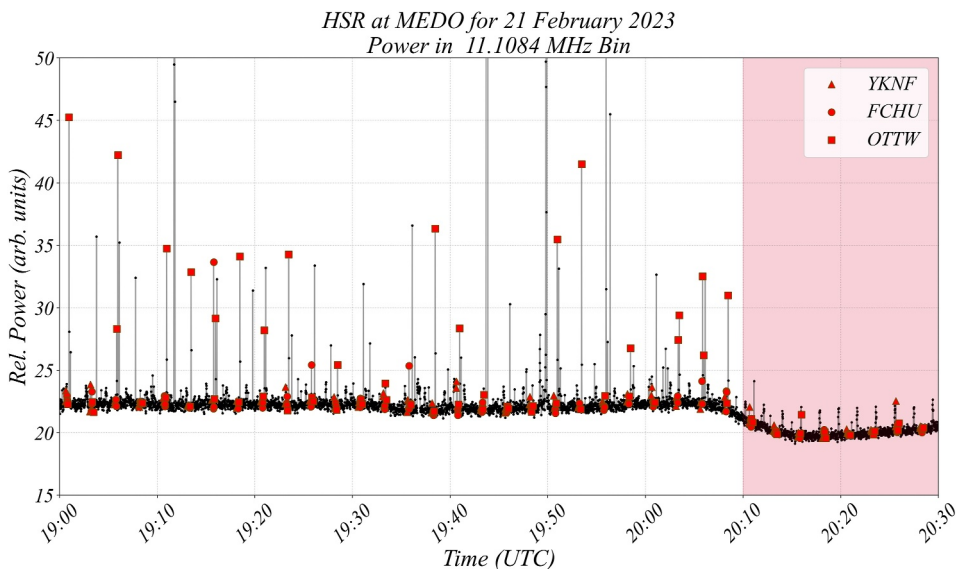


**Figure 11.** The observed power in the 11.1084 MHz bin corresponding to the 11.107 MHz band in which Natural Resources Canada transmits. Known transmission times for YKNF, FCHU, and OTTW are marked by red triangles, circles, and rectangles, respectively. Observed is an instantaneous loss of the OTTW transmissions at the time of the event, highlighted in red.

close proximity indicate a higher likelihood that the same absorbing region was responsible for the loss of the rays associated with those pierce points.

## 5. Discussion

We have presented here, a methodology to leverage terrestrial HF information contained in new Hyper-Spectral Riometers (slated to replace existing GO-Canada single frequency systems in the 2024–2025 timeframe) and provide information about spatial extent of electron density enhancements. Our methodology allows for estimation of the geographic extent of D-region enhancements under certain conditions. We note that this methodology does not allow for exploration of the dynamics within the absorbing region, since once the terrestrial signal is lost there is no further information. Therefore, the structuring within the absorbing region, or information about its temporal dynamics are not available. We do however note that information from the initial loss of terrestrial HF signals from within the riometer data can provide valuable information about instantaneous sizes along multiple axes (e.g., AA precipitation region, boundary of the polar cap). Here we have shown one such example, from the prototype SWAN HSR data, where we utilized information about 4 known HF transmitters to infer the size of an assumed absorbing layer associated with a region of enhanced D-region electron density. We have found that the methodology provided a consistent picture of the extent of D-region electron density enhancements when compared amongst 2 different HSRs. The spatial extent derived is also consistent with expected behavior of riometer spatial scales and impact region for HF dropout due to the solar flare event (Frissell et al., 2014).

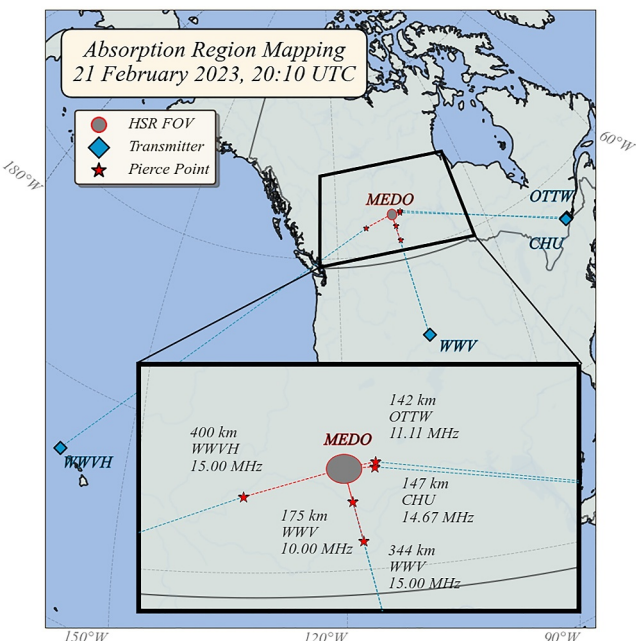


**Figure 12.** Map showing the pierce-point of the rays that reach the riometer prior to absorption onset for the event on 21 February 2023. Ray traces were performed at 20:10 UT and 7.85 MHz for CHU, 10 and 15 MHz for WWVH and WWVH, and 11.107 MHz for NRCan's Ottawa (OTTW) and transmitter. The HSR's FOV is projected to 85 km altitude.

An absorbing layer height of 85 km was assumed in the generation of the pierce point map shown in Figure 14. The actual height of peak absorption can vary depending on the absorption mechanism. Studies using radars in conjunction with riometers indicate that the height of peak absorption (AA) typically falls within the 85–95 km altitude range, with 50% levels relative to

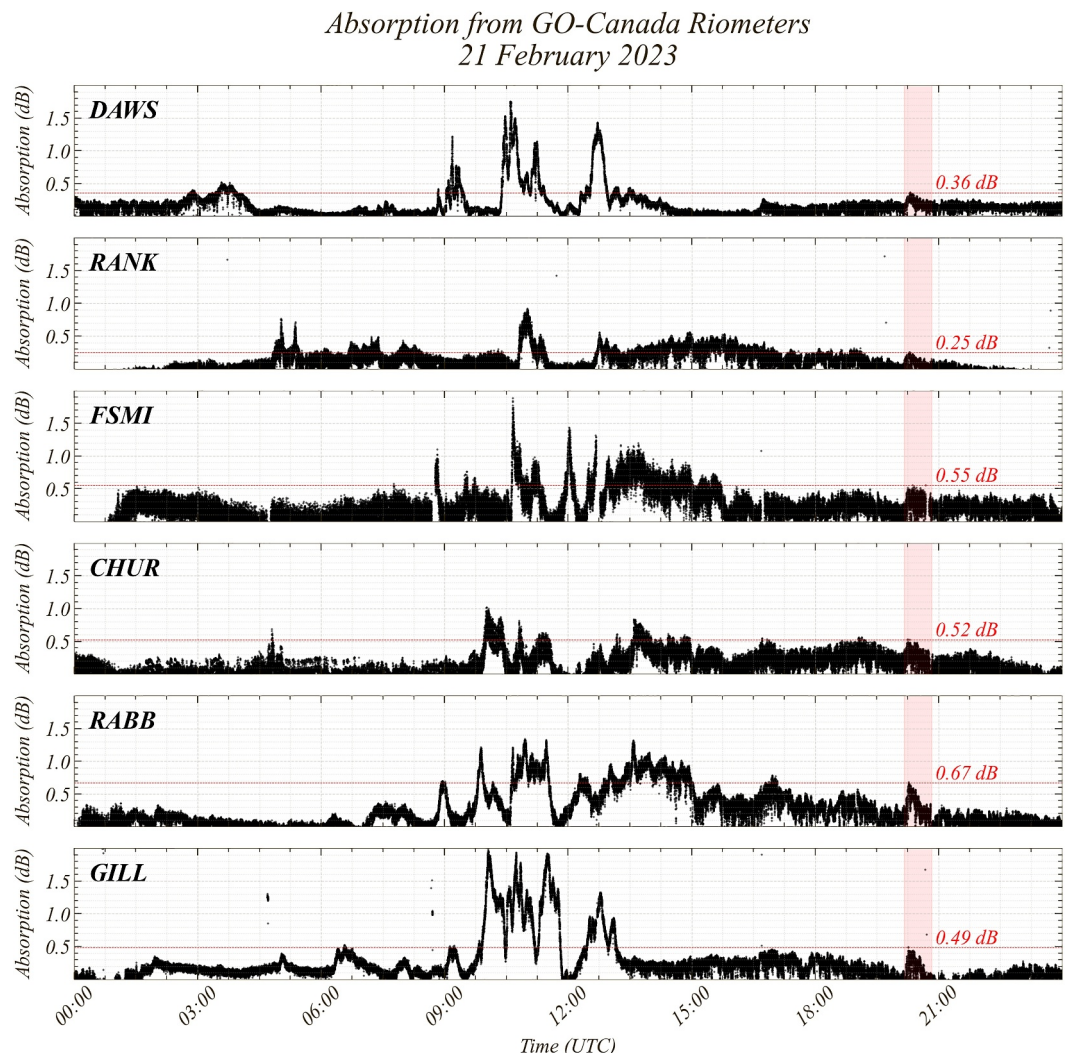


**Figure 13.** Absorption measurements from the GO-Canada riometers for the day of the 21 February 2023. Peak absorption during the time of the event (highlighted in red), is shown by a horizontal red line along with the measurement of peak absorption above it (written in red). The site code is displayed on the top left corner of each plot.

the maximum falling between about 5 and 20 km (Burns et al., 1990; Devlin et al., 1986; Hargreaves, 1980; Hargreaves & Devlin, 1990; Hargreaves et al., 2007). There are some extreme cases where AA can penetrate much deeper (Collis et al., 1996). For AA, assuming 85 km would be most suitable as it is the minimum of the aforementioned range. However, the assumption for the slab's altitude may differ for different events, for example, being lower, between 45 and 65 km, for daytime PCA events (e.g., Hargreaves, 2005; Kavanagh et al., 2004) as compared to AA (Rees, 1963, 1964). For flares, the base of the enhanced D-region is generally below ~70 km, decreasing with increasing flare intensity (McRae & Thomson, 2004; Mitra, 1974).

The choice of slab height is critical to the methodology presented here. In general, that decision will be informed by the type of event (as discussed above). For certain events (e.g., nightside AA or flares), multiple riometers can be employed to elucidate the temporal and spatial nature of the riometer signatures (e.g., Fiori et al., 2018; Spanswick et al., 2007), and inform the choice of slab height based on an assumed source of D-region enhancement. In addition, data from other sources can be used to inform the methodology where appropriate. For example, for the event presented here, we confirmed the presence of a flare utilizing the GOES X-ray flux.

The slab height and ionospheric model are the two largest sources of error within this technique. Table 3 can be used to estimate the error due to slab height, with an approximate 27 km difference in range determination for

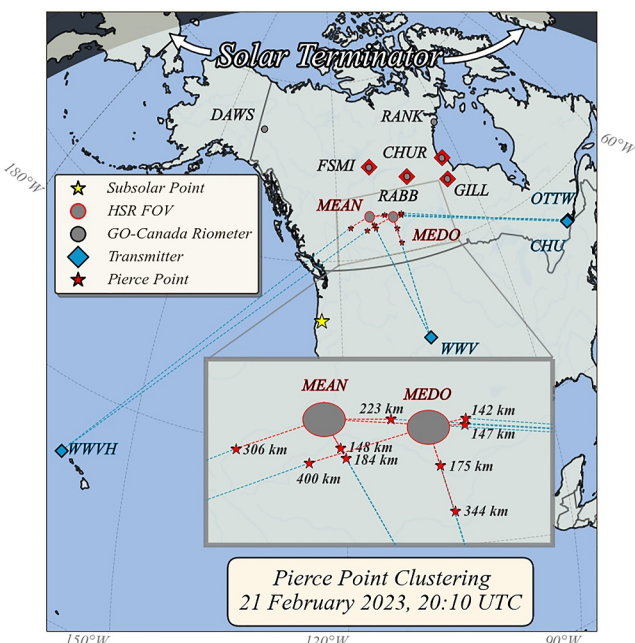


**Figure 14.** Map showing the pierce points extracted via applying our methodology to both the Meanook (MEAN) and Meadow (MEDO) Hyperspectral Riemometers. The clustering of pierce points defines the boundary of the absorbing region. GO-Canada riometers, shown as gray circles with black boundaries, have been added to the map. Additionally, GO-Canada riometers with peak absorption of 0.5 dB or higher are marked with a red diamond behind the gray circle. The subsolar point is shown as a yellow star and the boundary of the solar terminator is marked by the shaded region. The distance from each riometer to different pierce points (red dashed lines) is indicated next to each pierce point. One pierce point connecting CHU to MEAN is located within MEDO's FoV.

every 10 km of altitude difference in the slab height. Some of this can be mitigated by utilizing more than one frequency from a given transmitter. Rays with higher angle-of-arrival generally require more hops and pierce the D-region closer to the riometer. Therefore, the low-angle rays provide the upper limit on the absorption distance. Often, both a range of high-angle and low-angle rays can provide viable links. The clustering of pierce points across frequency can therefore provide confidence for the spatial structure of the absorbing region. Other errors will occur via the modeling of the ray reflection height, which is a function of the modeled ionospheric electron density. We assert it is minimized here since the model is utilized to determine signal reception prior to the disturbance. Other models, such as tomographic data assimilative models, will be utilized in future work. Other mitigation of error will occur as more HSRs and transmitters are added to the network, providing estimates from multiple locations and directions.

Our methodology provides pierce point locations beyond the FoV which could be beneficial for over-the-horizon radars and directional HF systems, particularly because wide-beam riometers would miss absorption patches that have crossed the nominal FoV (Birch et al., 2013). Highly localized enhancements, such as the spike event as observed by riometers (Hargreaves et al., 1979; Spanswick et al., 2005), can be mitigated via channel change. Although, if the HF circuit passes through the spike region, the absorption can be abnormally high, which is often underestimated by wide-beam riometers (Burns et al., 1990; Hargreaves, 1980; Hargreaves et al., 1991, 1997) and there is even evidence that the spatial scales of such structures can be less than that of imaging systems' beam width over small time-scales (Hargreaves et al., 2007). While localized absorption can be more-easily mitigated, widespread absorption that targets multiple areas simultaneously such as the SWF event discussed in this study, or PCA events, may be harder to mitigate (Frissell et al., 2014; Hunsucker & Hargreaves, 2003). A shift to higher frequencies is advised, since the absorption gradually shifts to enhancement as the operating frequency shifts toward the Very HF range (Mitra, 1974).

## 6. Conclusions

Prototype data from the SWAN Hyper-Spectral Riemometers have proven capable of capturing a time-series of power from known terrestrial transmitters in addition to nominal cosmic noise. In combination with cosmic absorption and ray tracing, we use a simple methodology to analyze HF link status information and derive a minimum size of the D-region enhancement under certain assumptions some of which are discussed in Section 5.

While only in the prototype stage, this methodology could be utilized in future studies to explore the evolution of the HF environment in consort with more advanced models of the ionospheric electron density and leveraging the known response of the riometer to D-region electron density enhancements. Having the two capabilities on a unified platform, from an extended array of riometers, will provide significant information about overall spatial extent with numerous intersecting terrestrial signal paths for validation. Details of the time of signal loss for different frequencies in comparison to the onset of overhead cosmic absorption could also provide information about the motion of D-region electron enhancements prior to complete terrestrial signal loss. Future work will include further exploration of the signal timings for events with multiple riometers when there is observed motion between two riometers. We are also exploring incorporating this methodology into more comprehensive ionospheric electron density models, such as GNSS tomographic inversions.

## Data Availability Statement

The raw data from the Canadian riometers are available from the University of Calgary Space Physics Data portal ([https://data.phys.ucalgary.ca/sort\\_by\\_project/other/publication\\_datasets/2023JA032375](https://data.phys.ucalgary.ca/sort_by_project/other/publication_datasets/2023JA032375)).

## Acknowledgments

The SWAN riometers are funded by the Canada Foundation for Innovation, the Province of Alberta, and the University of Calgary. Operational support is provided by the Canadian Space Agency and Space Environment Canada. The results published in this paper were obtained using the HF propagation toolbox, PHARLAP, created by Dr Manuel Cervera, Defence Science and Technology Group, Australia ([manuel.cervera@dsto.defence.gov.au](mailto:manuel.cervera@dsto.defence.gov.au)). This toolbox is available by request from its author. This is NRCan publication 20230330. We also gratefully acknowledge support from the U.S. National Science Foundation under Grants 1229541 and 1248062.

## References

- Ads, A. G., Bergadà, P., Regué, J. R., Alsina-Pagès, R. M., Pijoan, J. L., Altadill, D., et al. (2015). Vertical and oblique ionospheric soundings over the long haul HF link between Antarctica and Spain. *Radio Science*, 50(9), 916–930. <https://doi.org/10.1002/2015rs005773>
- Baker, D. N., Stauning, P., Hones, E. W., Jr., Higbie, P. R., & Belian, R. D. (1981). Near-equatorial, high-resolution measurements of electron precipitation at  $L \approx 6.6$ . *Journal of Geophysical Research*, 86(A4), 2295–2313. <https://doi.org/10.1029/JA086iA04p02295>
- Berkey, F. T., Driatskiy, V. M., Henriksen, K., Hultqvist, B., Jelly, D. H., Shchuka, T. I., et al. (1974). A synoptic investigation of particle precipitation dynamics for 60 substorms in IQSY (1964–1965) and IASY (1969). *Planetary and Space Science*, 22(2), 255–307. [https://doi.org/10.1016/0032-0633\(74\)90028-2](https://doi.org/10.1016/0032-0633(74)90028-2)
- Birch, M. J., Hargreaves, J. K., & Bromage, B. J. I. (2013). Properties of auroral radio absorption patches observed in the morning sector using imaging riometer and incoherent-scatter radar. *Journal of Atmospheric and Solar-Terrestrial Physics*, 105–106, 262–272. <https://doi.org/10.1016/j.jastp.2012.12.004>
- Blagoveshchensky, D. V., & Kalishin, A. S. (2009). Increase in the critical frequency of the ionospheric F region prior to the substorm expansion phase. *Geomagnetism and Aeronomy*, 49(2), 200–209. <https://doi.org/10.1134/S0016793209020091>
- Blagoveshchensky, D. V., & Sergeeva, M. A. (2020). Substorm manifestations at radio paths of oblique ionospheric sounding in the Arctic. *Pure and Applied Geophysics*, 177(10), 4971–4982. <https://doi.org/10.1007/s0024-020-02539-4>
- Bland, E., Bozoki, T., & Partamies, N. (2022). Spatial extent of the energetic electron precipitation region during substorms. *Frontiers in Astronomy and Space Sciences*, 9, 978371. <https://doi.org/10.3389/fspas.2022.978371>
- Bland, E., Tesema, F., & Partamies, N. (2021). D-region impact area of energetic electron precipitation during pulsating aurora. *Annales Geophysicae*, 39(1), 135–149. <https://doi.org/10.5194/angeo-39-135-2021>
- Budden, K. G. (1988). *The propagation of Radio Waves: The Theory of radio waves of low power in the ionosphere and magnetosphere* (pp. 7–17). Cambridge University Press.
- Burns, C. J., Howarth, W. G., & Hargreaves, J. K. (1990). High-resolution incoherent scatter radar measurements during electron precipitation events. *Journal of Atmospheric and Terrestrial Physics*, 52(3), 205–218. [https://doi.org/10.1016/0021-9169\(90\)90124-6](https://doi.org/10.1016/0021-9169(90)90124-6)
- Cameron, T. G., Fiori, R. A. D., Warrington, E. M., Stocker, A. J., Thayaparan, T., & Danskin, D. W. (2021). Characterization of high latitude radio wave propagation over Canada. *Journal of Atmospheric and Solar-Terrestrial Physics*, 219, 105666. <https://doi.org/10.1016/j.jastp.2021.105666>
- Canada, N. R. C. (2019). *Government of Canada*. National Research Council Canada. Retrieved from <https://nrc.ca/en/certifications-evaluations-standards/canadas-official-time/nrc-shortwave-station-broadcasts-chu>
- Chakraborty, S., Baker, J. B. H., Fiori, R. A. D., Ruohoniemi, J. M., & Zawdie, K. A. (2021). A modeling framework for estimating ionospheric HF absorption produced by solar flares. *Radio Science*, 56(10), e2021RS007285. <https://doi.org/10.1029/2021RS007285>
- Collis, P. N., Hargreaves, J. K., & White, G. P. (1996). A localised co-rotating auroral absorption event observed near noon using imaging riometer and EISCAT. *Annales Geophysicae*, 14(12), 1305–1316. <https://doi.org/10.1007/s00585-996-1305-y>
- Danilov, A. D. (2013). Ionospheric F-region response to geomagnetic disturbances. *Advances in Space Research*, 52(3), 343–366. <https://doi.org/10.1016/j.asr.2013.04.019>
- Davies, K. (1990). Ionospheric Radio, P. Peregrinus on behalf of the. Institution of Electrical Engineers.
- Devlin, T., Hargreaves, J. K., & Collis, P. N. (1986). Eiscat observations of the ionospheric D-region during auroral radio absorption events. *Journal of Atmospheric and Terrestrial Physics*, 48(9), 795–805. [https://doi.org/10.1016/0021-9169\(86\)90054-1](https://doi.org/10.1016/0021-9169(86)90054-1)
- Fiori, R. A. D., Chakraborty, S., & Nikitina, L. (2022). Data-based optimization of a simple shortwave fadeout absorption model. *Journal of Atmospheric and Solar-Terrestrial Physics*, 230, 105843. <https://doi.org/10.1016/j.jastp.2022.105843>
- Fiori, R. A. D., Koustov, A. V., Chakraborty, S., Ruohoniemi, J. M., Danskin, D. W., Boteler, D. H., & Shepherd, S. G. (2018). Examining the potential of the super dual auroral radar network for monitoring the space weather impact of solar X-ray flares. *Space Weather*, 16(9), 1348–1362. <https://doi.org/10.1029/2018SW001905>
- Fiori, R. A. D., Kumar, V. V., Boteler, D. H., & Terkildsen, M. B. (2022). Occurrence rate and duration of space weather impacts on high-frequency radio communication used by aviation. *Journal of Space Weather and Space Climate*, 12, 21. <https://doi.org/10.1051/swsc/2022017>
- Frissell, N. A., Miller, E. S., Kaepller, S. R., Ceglia, F., Pascoe, D., Sinanis, N., et al. (2014). Ionospheric sounding using real-time amateur radio reporting networks. *Space Weather*, 12(12), 651–656. <https://doi.org/10.1002/2014SW001132>
- Froñ, A., Galkin, I., Krankowski, A., Bilitza, D., Hernández-Pajares, M., Reinisch, B., et al. (2020). Towards cooperative global mapping of the ionosphere: Fusion feasibility for IGS and IRI with global climate VTEC maps. *Remote Sensing*, 12(21), 3531. <https://doi.org/10.3390/rs1213531>
- Hargreaves, J. K. (1969). Auroral absorption of HF radio waves in the ionosphere: A review of results from the first decade of riometry. *Proceedings of the IEEE*, 57(8), 1348–1373. <https://doi.org/10.1109/proc.1969.7275>
- Hargreaves, J. K. (1980). D-region electron densities observed by incoherent-scatter radar during auroral-absorption spike events. *Journal of Atmospheric and Terrestrial Physics*, 42(9), 783–789. [https://doi.org/10.1016/0021-9169\(80\)90081-1](https://doi.org/10.1016/0021-9169(80)90081-1)
- Hargreaves, J. K. (2005). A new method of studying the relation between ionization rates and radio-wave absorption in polar-cap absorption events. *Annales Geophysicae*, 23(2), 359–369. <https://doi.org/10.5194/angeo-23-359-2005>
- Hargreaves, J. K., Birch, M. J., & Bromage, B. J. I. (2007). D- and E-region effects in the auroral zone during a moderately active 24-h period in July 2005. *Annales Geophysicae*, 25(8), 1837–1849. <https://doi.org/10.5194/angeo-25-1837-2007>
- Hargreaves, J. K., Browne, S., Ranta, H., Ranta, A., Rosenberg, T. J., & Detrick, D. L. (1997). A study of substorm-associated nightside spike events in auroral absorption using imaging riometers at South Pole and Kilpisjärvi. *Journal of Atmospheric and Solar-Terrestrial Physics*, 59(8), 853–872. [https://doi.org/10.1016/S1364-6826\(96\)00061-2](https://doi.org/10.1016/S1364-6826(96)00061-2)
- Hargreaves, J. K., Chivers, H. J. A., & Nielsen, E. (1979). Properties of spike events in auroral radio absorption. *Journal of Geophysical Research*, 84(A8), 4245–4250. <https://doi.org/10.1029/JA084iA08p04245>
- Hargreaves, J. K., Detrick, D. L., & Rosenberg, T. J. (1991). Space-time structure of auroral radio absorption events observed with the imaging riometer at south pole. *Radio Science*, 26(4), 925–930. <https://doi.org/10.1029/91RS00179>
- Hargreaves, J. K., & Devlin, T. (1990). Morning sector electron precipitation events observed by incoherent scatter radar. *Journal of Atmospheric and Solar-Terrestrial Physics*, 52(3), 193–203. [https://doi.org/10.1016/0021-9169\(90\)90123-5](https://doi.org/10.1016/0021-9169(90)90123-5)
- Hunsucker, R., & Hargreaves, J. (2003). *The high-latitude ionosphere and its effects on radio propagation*. Cambridge University Press.
- Hunsucker, R. D., & Bates, H. F. (1969). Survey of polar and auroral region effects on HF propagation. *Radio Science*, 4(4), 347–365. <https://doi.org/10.1029/RS004i004p00347>
- Jones, S. L., Lessard, M. R., Rychert, K., Spanswick, E., & Donovan, E. (2011). Large-scale aspects and temporal evolution of pulsating aurora. *Journal of Geophysical Research*, 116(A3). <https://doi.org/10.1029/2010JA015840>

- Kainuma, S., Ishii, M., Murayama, Y., Kikuchi, T., Mori, H., & Igarashi, K. (2001). Drift motion of ionospheric arc-like absorption regions observed with a 256-beam imaging riometer in Alaska. *Earth Planets and Space*, 53(7), 753–760. <https://doi.org/10.1186/bf03352403>
- Kavanagh, A. J., Marple, S. R., Honary, F., McCrea, I. W., & Senior, A. (2004). On solar protons and polar cap absorption: Constraints on an empirical relationship. *Annales Geophysicae*, 22(4), 1133–1147. <https://doi.org/10.5194/angeo-22-1133-2004>
- LaBelle, J., Weatherwax, A. T., Trimpie, M. L., Brittain, R., Hunsucker, R. D., & Olson, J. V. (1994). The spectrum of LF/MF/HF radio noise at ground level during substorms. *Geophysical Research Letters*, 21(24), 2749–2752. <https://doi.org/10.1029/94gl02513>
- Makarevitch, R. A., Honary, F., McCrea, I. W., & Howells, V. S. C. (2004). Imaging riometer observations of drifting absorption patches in the morning sector. *Annales Geophysicae*, 22(10), 3461–3478. <https://doi.org/10.5194/angeo-22-3461-2004>
- McRae, W. M., & Thomson, N. R. (2004). Solar flare induced ionospheric D-region enhancements from VLF phase and amplitude observations. *Journal of Atmospheric and Solar-Terrestrial Physics*, 66(1), 77–87. <https://doi.org/10.1016/j.jastp.2003.09.009>
- Milan, S. E., Jones, T. B., & Warrington, E. M. (1997). Enhanced MUF propagation of HF radio waves in the auroral zone. *Journal of Atmospheric and Solar-Terrestrial Physics*, 59(2), 237–248. [https://doi.org/10.1016/S1364-6826\(96\)00031-4](https://doi.org/10.1016/S1364-6826(96)00031-4)
- Milan, S. E., Jones, T. B., Warrington, E. M., & Reeves, G. D. (1994). Observations of substorm associated absorption events on a 3200 km high latitude HF propagation path. In *1994 sixth international conference on HF radio systems and techniques* (pp. 69–73).
- Milan, S. E., Lester, M., Jones, T. B., & Warrington, E. M. (1998). Observations of the reduction in the available HF band on four high latitude paths during periods of geomagnetic disturbance. *Journal of Atmospheric and Solar-Terrestrial Physics*, 60(6), 617–629. [https://doi.org/10.1016/S1364-6826\(98\)00005-4](https://doi.org/10.1016/S1364-6826(98)00005-4)
- Mitra, A. P. (1974). *Ionospheric effects of solar flares*. Reidel.
- Nelson, G. K., Lombardi, M. A., & Okayama, D. T. (2005). *NIST time and frequency radio stations: WWV, WWVH, and WWVB*. NIST Special Publication. Retrieved from <https://www.nist.gov/system/files/documents/calibrations/sp250-67.pdf>
- Rees, M. H. (1963). Auroral ionization and excitation by incident energetic electrons. *Planetary and Space Science*, 11(10), 1209–1218. [https://doi.org/10.1016/0032-0633\(63\)90252-6](https://doi.org/10.1016/0032-0633(63)90252-6)
- Rees, M. H. (1964). Note on the penetration of energetic electrons into the earth's atmosphere. *Planetary and Space Science*, 12(7), 722–725. [https://doi.org/10.1016/0032-0633\(64\)90236-3](https://doi.org/10.1016/0032-0633(64)90236-3)
- Spanswick, E., Donovan, E., Liu, W., Wallis, D., Aasnes, A., Hiebert, T., et al. (2005). Substorm associated spikes in high energy particle precipitation. In *The inner magnetosphere: Physics and modeling* (pp. 227–236). American Geophysical Union (AGU). <https://doi.org/10.1029/155GM24>
- Spanswick, E., Friedel, R., & Korth, A. (2007). Ground based identification of dispersionless electron injections. *Geophysical Research Letters*, 34(3). <https://doi.org/10.1029/2006GL028329>
- Uryadov, V. P., Vybornov, F. I., & Pershin, A. V. (2019). Features of the HF signal propagation on oblique sounding paths during solar and magnetic activity in September 2017. *Radiophysics and Quantum Electronics*, 62(2), 85–98. <https://doi.org/10.1007/s11141-019-09956-z>
- Weatherwax, A. T., LaBelle, J., Trimpie, M. L., Brittain, R., & Treumann, R. A. (1994). Ground-based observations of MF/HF radio noise in the auroral zone. *Journal of Geophysical Research*, 99(A2), 2109–2119. <https://doi.org/10.1029/93JA01806>